# Large Eddy Simulation of boundary layer transition over an isolated ramp-type micro roughness element

Hatim Belkhou, Serge Russeil, Talib Dbouk, Mohammed Mobtil, Daniel Bougeard, Nicolas-Yoan Francois

Version of Record: https://www.sciencedirect.com/science/article/pii/S0142727X19306289
Manuscript_4f295e8ccdf82d2c19db74837e57c582

# Large Eddy Simulation of boundary layer transition over an isolated ramp-type micro roughness element

Hatim Belkhou[a,*], Serge Russeil[a], Talib Dbouk[a], Mohammed Mobtil[a], Daniel Bougeard[a], Nicolas-Yoan Francois[b]

[a] *IMT Lille Douai, Energy Engineering Department, F59500 Douai, France*
[b] *VALEO Thermal Systems, 8 rue Louis Lormand, F78321 La Verriere, France*

**Abstract**

Boundary layer transition over an isolated surface roughness element is investigated by means of numerical simulation. Large Eddy Simulation (LES) flow-modeling approach is employed to study flow characteristics and transition phenomenon past a roughness element immersed within an incoming developing boundary layer, at a height-based Reynolds number of 1170. LES numerical results are compared to experimental data from literature showing the time-averaged velocity distribution, the velocity fluctuation statistics and the instantaneous flow topology.

Despite slight difference in the intensity of streamwise velocity fluctuations, the present LES results and experimental data show very good agreement. The mean flow visualization shows streamwise counter-rotating vortices pairs formation downstream of the obstacle. The primary pair induces an upwash motion and a momentum deficit that creates a Kelvin-Helmholtz type flow instability. The instantaneous flow topology reveals the formation of coherent K-H vortices downstream that produce turbulent fluctuations in the wake of the roughness element. These vortices are streched and lifted up when moving downstream. The velocity fluctuations results show that the onset of the turbulence is dominated by the energy transfer of large-scale vortices.

*Corresponding author
*Email address:* hatim.belkhou@imt-lille-douai.fr (Hatim Belkhou)

*Keywords:* LES, Boundary layer, CFD, Hairpin vortices, Roughness element, Laminar-turbulent transition

## 1. Introduction

Boundary layer transition is a known phenomenon occurring in a large range of industrial configurations and applications, and thus its prediction is of major importance and remains a crucial issue.

In a developing boundary layer flow, the transition regime from laminar to turbulent is an uncertainty state, which makes the boundary layer transition prediction a major subject of many studies. The flow over a smooth flat plate is expected to remain laminar until a certain distance range from the leading edge, but the presence of roughness structures triggers instabilities that can cause significant momentum transport. In separation control applications and aero-thermal problems theses disturbances and their impact on the momentum distribution normal to the wall are of great importance. Thus, the interaction between a boundary layer and structures immersed in it represents an interesting and complex problem.

The effect of roughness elements in promoting boundary layer transition is commonly [1, 2, 3] linked to the height-based Reynolds number. This Reynolds number considers the roughness size as a characteristic length, so a roughness element with large enough size may greatly modify the transition mechanism for a developing laminar boundary layer, and accelerate the transition process.

Till now, the structure details and creation of the turbulent-like boundary layers induced by different types of roughness elements are still not very well understood and analyzed.

Various flow disturbances may trigger this transition and act as an accelerating process source (i.e. natural, bypass, etc.). These disturbances are the sources of complex mechanisms which finally lead to turbulence. There are three main paths to turbulence:

- Natural: for smooth walls and flows with extremely low levels of dis-

turbances (freestream turbulence, vibrations, etc.), boundary layer can remain laminar well beyond critical Reynolds values for bypass transition. The transition results in this case from the amplification of unstable waves.

- Bypass: sufficient disturbances are present (such as in most engineering applications), so the flow transition occurs spontaneously and far upstream the natural transition location. In this case, the waves are no longer present and other instability structures are observed.
- Induced: It means that the laminar-to-turbulent transition is triggered by an element (wall-mounted obstacle, wall-roughness, etc.), which leads to instabilities and a rapid breakdown to turbulence.

In very common engineering applications, a wide range of heat exchangers are often used with complex surface geometries (surface obstacles used to enhance the overall efficiency), at various types of fluid and flow regimes. One of the major challenges in this framework is then to correctly model and simulate correctly the laminar-turbulent transition and thus capture the real physics behind. Indeed, laminar-to-turbulent transition can greatly influence several flow parameters like the pressure drop, drag coefficient and heat transfer efficiency. Hence it is very important to understand these transition phenomenon in order to predict well transition processes.

For modeling transitional and turbulent flows, the Reynolds-Averaged Navier-Stokes (RANS) approach is one strategy mainly used for its reasonable computational time and simplified post-processing [4, 5]. The ability of RANS simulations to capture the laminar-to-turbulent transition is very limited and depends mainly on the flow unsteadiness and the predictive capability of the turbulence models.

In the work of Toubiana *et al.*[6], three modeling approaches were employed to study the evolution of three-dimensional transitional and turbulent flow characteristics and heat transfer in staggered plate arrays. Laminar, RANS and LES simulation have been compared for various Reynolds number ranging from 300 to 9000. A very significant deviation, up to 44% for friction factor and 27%

for Colburn factor, in the transitional regime has been found when comparing all numerical approaches, showing that the various laminar and RANS models have great difficulties to predict the laminar-to-turbulent transition.

Zhang *et al.*[7] conducted numerical analysis of the unsteady behavior of transitional fluid flow and heat transfer in a plate-fin and tube heat exchanger. The numerical results were compared to experimental results for the baseline plate-fin and tube heat exchanger for Reynolds number from 978 to 2257. Laminar, RANS standard $k-\varepsilon$ (SKE) and LES approaches were used to simulate the transitional flow for a wide range of fin pitches. It has been found that the SKE model overestimates the heat transfer by at least 50% for all Reynolds numbers. The laminar model shows good agreement for Reynolds numbers below 1000. The LES is the only appropriate model for the analysis of flow and heat transfer in the transitional flow regime, where the laminar and SKE models failed.

Thus regarding the numerical studies of transitional flows, various RANS turbulence models were applied and showed their inability to accurately predict the transition location and its properties. Laminar to turbulent transition owing to instability processes cannot be predicted by statistical RANS models that average the turbulent structures. Thus, none of the turbulent structures are resolved in the RANS approach, and the Large Eddy Simulation (LES) appears as an interesting approach allowing to explicitly resolve a very wide range of time and eddies length scales (with DNS approach, which remains too costly for engineering applications).

However, it is important to note that some RANS-based turbulence models were designed to predict the laminar-turbulent transition. Malan [8] discusses the implementation and validation of the $\gamma - Re_\theta$, a Local Correlation based Transition Model (LCTM) based on the Shear Stress Transport (SST) $k-\omega$ model of Menter [9] widely used for engineering applications.

Although the flow past obstacles and protrusions has been widely studied in turbulent and compressible boundary layers, supersonic and hypersonic flow regime [10, 11, 12, 13], surprisingly, the flow around an isolated obstacle immersed in a laminar and incompressible developing boundary layer has been

reported in literature only in a few papers.

Ye *et al.*[14] performed tomographic Particle Image Velocimetry (PIV) to study the influence of various isolated roughness elements on boundary layer transition at super-critical regime. Different roughness geometries mounted on a flat plate were studied, where the upcoming developing flow is laminar. The conducted PIV measurements enabled the analysis of the mean and instantaneous flow characteristics in the roughness wake. Flow instability is induced and leads to vortex systems generation and turbulent fluctuations, which are associated to the transition mechanism.

For similar flow configuration, Acarlar and Smith [15] undertook hot-film anemometry techniques to study discrete hairpin vortices and their induced flow patterns past a hemisphere protuberance placed in a stable developing laminar boundary. The authors concluded that the shear layer instability and related hairpin vortices play a significant role in the laminar-turbulent transition process, which confirms the PIV analysis of Ye *et al.*[14].

Yanaoka *et al.*[16] carried out three-dimensional direct numerical simulation (DNS) of a cube mounted on heated plate with an incoming laminar boundary layer to investigate the dynamics of the vortex structures formed in the wake and their impact on heat transfer. The numerical calculations were performed for a Reynolds number of 500 based on the cube size. A horseshoe and hairpin vortex system are generated behind the cube.

Diaz-Daniel *et al.*[17] studied the flow past wall-attached cube immersed in laminar and turbulent boundary layers by means of DNS at various Reynolds numbers. The flow mechanisms and structures generated downstream of the wall-attached cube are analyzed through turbulence energy spectra. It was found that the flow around a wall-attached cube strongly depends on the upstream flow conditions and generates an additional low-frequency far-field peak for turbulent incoming boundary layers.

The state of knowledge regarding the induced flow transition process past an immersed isolated roughness is limited. For theses cases, the details of the laminar-turbulent transition onset and evolution are still in question. The case

of an isolated wall-mounted roughness, although simplistic, may represent a reference scenario for incompressible boundary layer transition induced by an immersed obstacle. Such flows are encountered in various engineering applications (automotive heat exchangers, HVAC heat exchangers, airfoils, etc.).

One of the main objectives of the present paper is to develop and validate a numerical methodology based on Large Eddy Simulation (LES) technique, by comparing numerical results to experimental data obtained by tomographic PIV [14, 18]. The LES approach is then used for an extensive analysis of the induced transitional regime focusing on the mean and instantaneous flow organization as well as the turbulent statistics.

## 2. Simulations overview

The developing air flow over a flat plate equipped with an isolated roughness element is investigated. The geometry of the protrusion studied in the present paper follows the experimental work previously published by Ye *et al.*[14], that is the micro-ramp. The roughness element with a height of 2mm and a span width of 4mm is placed at 290mm from the leading edge inside a developing laminar boundary layer flow. The air freestream velocity $u_\infty$ is equal to 10 m/s, which is equivalent to a local Reynolds number of $Re_x = 176,000$ calculated at the roughness streamwise position. It indicates a laminar regime upstream the roughness position. It is worth to note that the roughness element is immersed within the laminar boundary layer: the ratio between the roughness height and the undisturbed boundary-layer thickness is $h/\delta_{99} = 0.61$. In such wall-mounted obstacle configuration, the height-based Reynolds number, i.e. $Re_h = \frac{h.u_\infty}{\nu}$, is often taken as a criterion for being in sub- or super-critical regime. In [1], it was established that the critical Reynolds number for an isolated roughness element ranges from 600 to 900 times aspect ratio power 0.4: $(h/c)^{0.4}$ (from 455 to 682 for an aspect ratio of 0.5). The simulations were carried out at a Reynolds number of 1170 based on the roughness height, indicating a supercritical regime.

*2.1. Mathematical model*

In order to perform a precise study of the transitional flow past roughness element, LES calculations are carried out using finite volume approach by means of the CFD software STAR-CCM+ 12.02 ®. The following considerations were made:

- three-dimensional and unsteady flow,
- isothermal flow,
- constant fluid (air) properties,
- negligible gravity and compressibility effects.

The LES approach resolves explicitly the large scales of turbulence while modeling the small scale motions, by means of a filtering operation applied to the Navier-Stokes equations. The governing equations of the present flow are the three-dimensional, unsteady, incompressible filtered Navier Stokes equations, given by:

$$\frac{\partial \rho}{\partial t} + \frac{\partial}{\partial x_i}(\rho \widetilde{u_i}) = 0 \tag{1}$$

$$\frac{\partial}{\partial t}(\rho \widetilde{u_i}) + \frac{\partial}{\partial x_i}(\rho \widetilde{u_i}\widetilde{u_j}) = -\frac{\partial \widetilde{p}}{\partial x_i} + \frac{\partial \sigma_{ij}}{\partial x_j} - \frac{\partial \tau_{ij}^R}{\partial x_j} \tag{2}$$

where the stress tensor is defined as follows:

$$\sigma_{ij} = \left[\mu\left(\frac{\partial \widetilde{u_i}}{\partial x_j} + \frac{\partial \widetilde{u_j}}{\partial x_i}\right)\right] - \frac{2}{3}\mu\frac{\partial \widetilde{u_i}}{\partial x_i}\delta_{ij} \tag{3}$$

where $\tau_{ij}^R$ is the subgrid-scale stress tensor and represents the effect of the subgrid-scale motions on the resolved grid-scale velocities of the fluid [19].

$$\tau_{ij}^R = \rho\widetilde{u_i u_j} - \rho\widetilde{u_i}\widetilde{u_j} \tag{4}$$

Boussinesq approximation assumes the exchange of turbulent energy in the cascading process of eddies is analogous to that of molecular viscosity. The subgrid-scale tensor is thus modeled using the turbulent viscosity as following:

$$\tau_{ij}^R = 2\nu_t \widetilde{S}_{ij} + \frac{1}{3}\tau_{kk}\delta_{ij} \tag{5}$$

where $\widetilde{S}_{ij}$ is the filtered resolved strain-rate tensor ($= \frac{1}{2}\left(\frac{\partial \widetilde{u_i}}{\partial x_j} + \frac{\partial \widetilde{u_j}}{\partial x_i}\right)$).

In the present study, the subgrid-scale tensor is modeled by the Wall-Adapting Local Eddy-viscosity (WALE) model which is based on the square of the velocity gradient tensor and has a proper near wall behavior that takes into account the effects of strain and rotation rates [20]. The WALE subgrid scale model provides the following mixing-length type formula for the subgrid scale viscosity:

$$\nu_t = (C_w \Delta)^2 \frac{(s_{ij}^d s_{ij}^d)^{3/2}}{(\widetilde{S}_{ij}\widetilde{S}_{ij})^{5/2} + (s_{ij}^d s_{ij}^d)^{5/4}} \tag{6}$$

where $\Delta$ is the the filter width and $C_w$ the non-universal model coefficient. The deformation parameter is defined as:

$$s_{ij}^d = \frac{1}{2}\left(\widetilde{g}_{ij}^2 + \widetilde{g}_{ji}^2\right) - \frac{1}{3}\delta_{ij}\widetilde{g}_{kk}^2 \tag{7}$$

where $\widetilde{g}_{ij} = \frac{\partial \widetilde{u_i}}{\partial x_j}$.

### *2.2. Numerical Procedure*

#### *2.2.1. Computational Domain*

The studied geometry and computational domain are illustrated in figure 1. The roughness height (noted h) is set to 2mm and its span width (noted c) to 4mm.

The origin of the coordinate system is located at the center of the roughness element. The x, y, z axes correspond respectively to the streamwise, wall-normal and spanwise directions. The study is focused on the flow nearby the roughness element, and especially the flow topology in the wake. Therefore, the computational domain is chosen as a rectangular box with a length of 55h, based on the roughness height (h). The roughness element is installed 10h downstream of the inlet. The width of the domain is 20h and the height is set to 5h, allowing minimal influence of the boundary conditions applied to the domain sides. The choice of these values are based on the experimental region of interest chosen for flow topology visualization by [14], see for example the green dashed line in figure 1 which represents the limit for experimental measurement domain height.

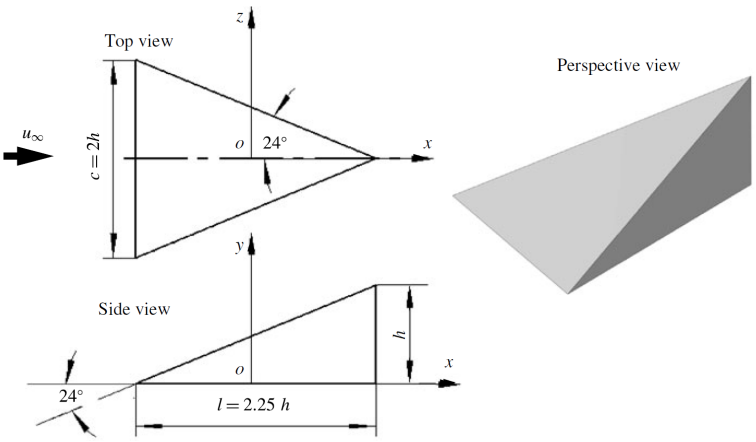


(a) Micro-ramp geometry and geometrical parameters (from [21])

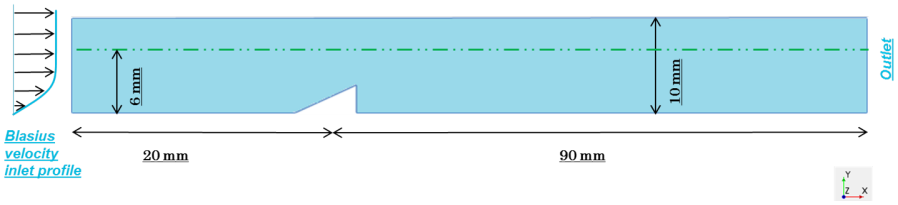


(b) Computational domain and boundary conditions

Figure 1: Roughness geometry and boundary conditions

In order to reduce the computational domain size, a two-dimensional laminar boundary layer profile is specified at the inlet boundary, which was set 270mm downstream the plate leading edge. The imposed profile is based on a Blasius boundary layer velocity profile [22]. At the outlet boundary, an outlet-pressure boundary condition with a fixed pressure value is imposed. No-slip conditions are assumed at the roughness and plate surfaces. The remaining boundaries are set to walls with a slip boundary condition on the velocity.

### *2.2.2. Grid generation*

A structured non-uniform mesh combined with a mesh refinement in the wake region and a near-wall refinement are applied. In order to maintain a smooth transition between the refined wake region and the domain complemen-

tary regions, transition regions are used. The detailed procedure of the wake refinement module can be found in the user guide [23]. Wall grid generation is applied to accurately capture the boundary layer and maximum $y^+$ is computed and found to be 0.96, thus respecting $y^+ < 1$. An example of the grid is shown in figure 2.

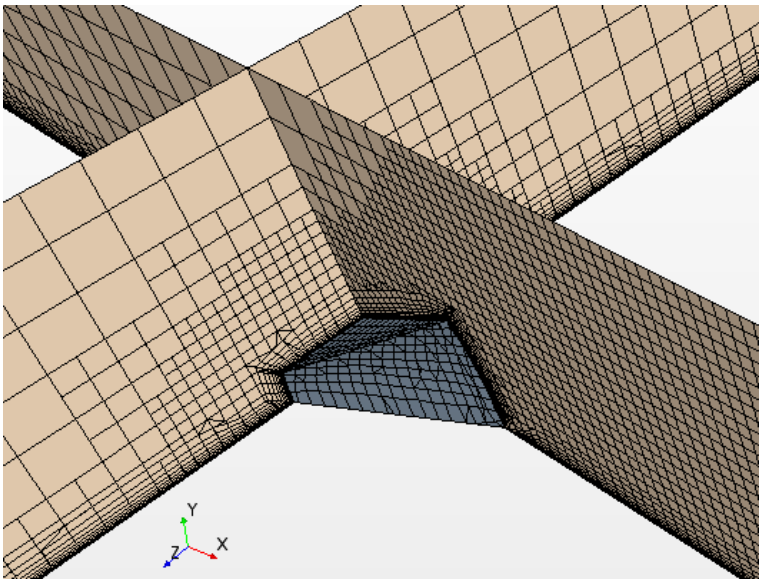


Figure 2: Schematic of the chosen grid.

A grid resolution study, to check the solution mesh-independence, was conducted using different three mesh sizes. The global skin friction coefficient is computed and used as a first indicator for the grid dependency. The refined mesh contains 7M cells. The coarse and medium meshes contain respectively 2.5M and 4.7M cells and the mean skin friction coefficient rate equals to 7.8% and 2.8% of the refined mesh mean skin friction coefficient. In this paper, the results based only on the 4.7M grid system are shown.

Moreover to further assess the mesh quality, we also adopted the most common criterion for LES found in the literature which is the index of resolution quality. This mesh quality index is defined as the ratio between the resolved turbulent kinetic energy and the total kinetic energy: $LES_{IQ} = \frac{k_{res}}{k_{tot}}$.

Celik [24] suggested an estimation of this ratio, based on the Kolmogorov scale as the following:

$$LES_{IQ_\eta} = \frac{1}{1 + a_\eta (\frac{h}{\eta_k})^m} \tag{8}$$

where $a_\eta$ and $m$ are two parameters that will be determined later. In first approximation: $h \approx V^{\frac{1}{3}}$, where V corresponds to the cell volume. The Kolmogorov scale is defined as: $\eta_k = (\frac{\nu^3}{\varepsilon})^{\frac{1}{4}}$, where $\varepsilon$ corresponds to the total dissipation rate. For the LES simulations, the total energy dissipation rate is computed as follows (sum of the resolved and modeled dissipation):

$$\varepsilon = \varepsilon_{res} + \varepsilon_{mod} = \frac{\nu + \nu_t}{2} \overline{(\frac{\partial u_i'}{\partial x_j} + \frac{\partial u_j'}{\partial x_i})^2} \tag{9}$$

In the literature, a LES simulation is usually considered as correctly resolved if 80% of the total kinetic energy is solved [25]. According to Pope [26], the motions responsible for the dissipation have a larger scale than the Kolmogorov scale, with a ratio of $8 < \frac{h}{\eta_k} < 60$, and a peak of dissipation of the turbulent kinetic energy located at $\frac{h}{\eta_k} = 25$.

As Celik [24] suggested, we consider that an index of resolution quality greater than 80% corresponds to a high-resolution LES and a value of 95% or more to a DNS. The parameters $a_\eta$ et $m$ are determined by considering, for example, that $h \simeq \eta_k$ corresponds to a Direct Numerical Simulation (DNS) and $h \simeq 25\eta_k$ to a LES. Thus, the parameters $a_\eta = 0.05$ / $m = 0.5$ are used in the study.

The local distribution of the index of resolution quality is shown in figure 3 for two characteristic planes. It is found that all IQ cell values are above 0.8 over the whole calculation domain. Thus, the considered mesh of 4.7M cells which details are shown in figure 2 was adopted for the present LES simulations.

*2.2.3. Numerical methods*

The equations governing the fluid flow are solved numerically using the Finite Volume Method (FVM) and the SIMPLE algorithm for pressure-velocity coupling [27]. Spatial derivatives are discretized using a second-order central

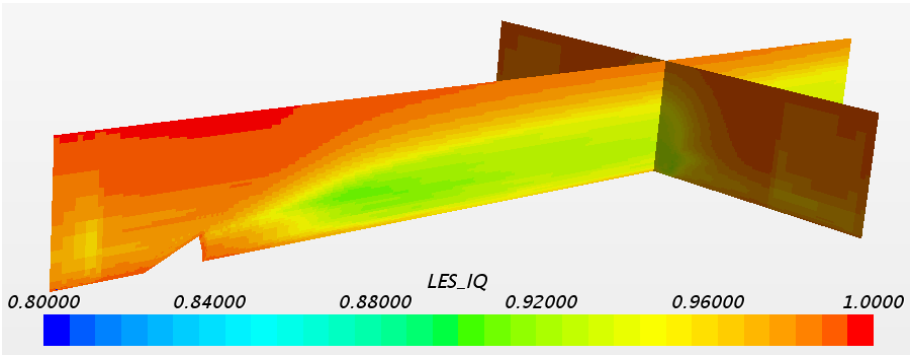


Figure 3: Index of resolution quality.

differencing scheme. An implicit second order scheme is employed for temporal discretization. The physical time step is carefully chosen to verify the Courant-Friedrichs-Lewy (CFL) condition ($CFL < 1$). The maximum Courant number value found over the entire calculation domain is around 1. Numerical convergence is verified by examining the residuals levels, mass balance and relevant quantities (wall shear, kinetic energy). Statistical convergence is obtained by monitoring pertinent quantities (Reynolds number based on mean friction velocity, volume-averaged turbulent kinetic energy). All simulations were initialized with the corresponding RANS simulation solution, and an integration of $500\frac{h}{u_\infty}$ time units was used to reach a state that is independent on the initial conditions. After an establishment period that ensures statistical convergence, data statistics for mean quantities are collected over 10,000 time steps (15 flow-through times) with a time step of $0.1\frac{h}{u_\infty}$. At each time step, solution convergence was achieved. It is worth to note that a convergence study for time averaging has been performed by comparing numerical results from a collection of 10,000 time steps and from an integration of 20,000 steps. Similar results of mean quantities were found, which consolidates our choice for this data processing time.

## 3. Time-averaged flow properties

### *3.1. Mean flow topology*

The mean flow topology is examined by visualizing the distribution of the mean streamwise velocity $\overline{u}$ over three cross-sectional planes y-z located downstream of the obstacle. Moreover, a projection of the velocity streamlines on these planes was applied. Figure 4 illustrates the comparison of the mean flow topology between the LES simulations and the PIV experimental results [14]. It should be mentioned that, in the present paper, the visualization domain of the LES simulation is adjusted so that its dimensions are equal to the experimental visualization domain (3hx10h). The mean streamwise velocity is normalized by the freestream magnitude.

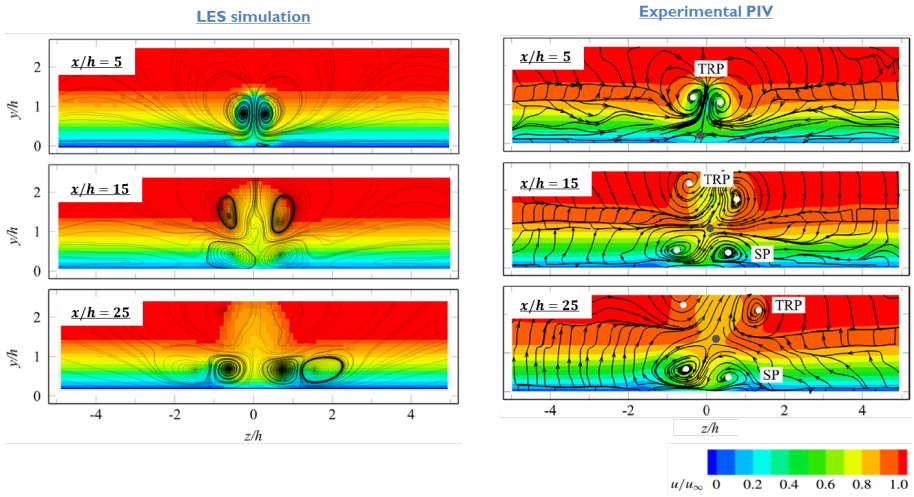


Figure 4: Color contours visualization of the non-dimensional mean velocity superimposed with projected streamlines at three streamwise positions y-z : x/h=5, 15, 25. (TRP) trailing-edge pair, (SP) secondary pair.

Downstream the obstacle, a pair of upwash vortices (TRP) is generated. In figure 4, a mushroom-like shape induced by the upwash movement as well as an axial velocity deficit in the plane of symmetry (z/h=0) are observed for both sets of results.

Moving downstream, the primary pair lifts up with a decrease of its intensity (x/h=15-25). As shown in figure 4, a second pair of induced counter-rotating vortices (SP) appears below the primary pair (x/h=15) in the near-wall vicinity. The formation of such a system of vortex pairs is also observed by Ye *et al.*[14]. The comparison between the LES and the PIV results shows a good agreement of the mean flow topology contours as well as the locations of the vortices at the different cross-sectional planes. It can be noticed that the downwash motion induced by the secondary pair produces a modification of the mean velocity profile in the symmetry plane (z/h=0): a velocity deficit at the saddle point located between the two pairs, below which the near-wall fluid is accelerated. The two swirling vortex pairs induces low and high momentum areas, corresponding to an increase of the shear stress which is associated with the generation of flow instabilities that leads to the transition from the laminar to the turbulent regime, as depicted in the following section.

### *3.2. Momentum deficit*

Further comparisons are made by analyzing the momentum deficit via the local mean streamwise velocity profiles. These profiles are plotted in figure 5, superimposed with the experimental profiles as well as the undisturbed flat plate profiles (Blasius laminar profiles).

The results show a momentum deficit of velocity approximately equal to $0.6u_\infty$ located at y/h = 1.2 at the position x/h=5. Consequently, a strong inflection point bounded with two shear layers is produced. The lower zone is produced under action of the secondary pair of vortices, which transports the fluid of high moment towards the symmetry plane. The upper zone is produced by the trailing edge pair of the obstacle. The latter shear layer induces Kelvin-Helmholtz type instabilities, which leads to the formation of vortex structures.

When moving downstream (x/h=15 and 40), a decrease of the mean streamwise velocity deficit is observed, and the profile tends to flatten. This decay indicates the presence of a recovery process across the boundary layer. This process is dominated by the mixing of large swirling scales, referred to as the

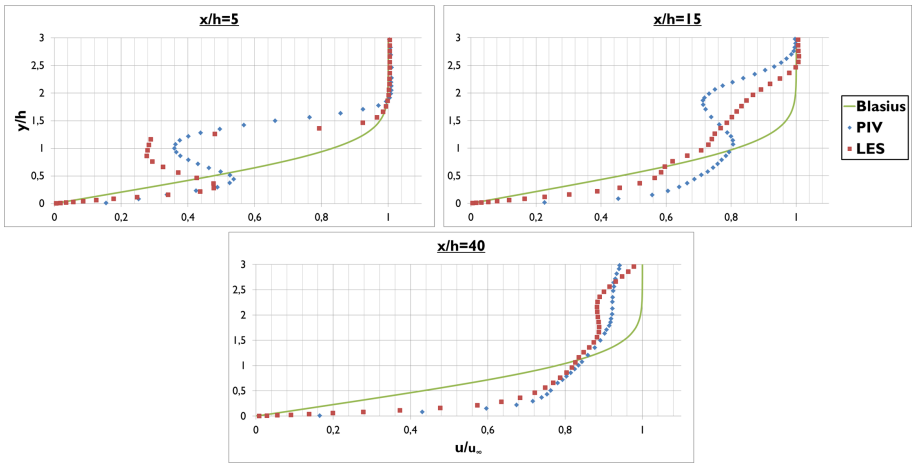


Figure 5: Profiles of mean streamwise velocity component in the center plane at three positions: x/h=5; 15; 40.

mixing layer. It should be noted that the deficit peak location (corresponding to a minimum of average axial velocity) moves upward when moving downstream. This movement is mainly attributable to the upwash motion of the main vortex structures (TRP, see figure 4). At the plane x/h=40, the intensity of the primary vortices is reduced and they are driven upwards by the upwash motion and are no longer detected within the visualization domain.

It can be seen from figure 5 that the recovery process is found to be slightly faster (between the planes x/h=5 and x/h=15) in the case of the numerical simulation LES compared to the experimental data [18].

In order to quantify this momentum recovery process, a maximum velocity deficit rate is defined as the following: $\frac{|\overline{u}(y)-\overline{u}_{BL}(y)|_{max}}{u_\infty}$, where $\overline{u}_{BL}$ is the Blasius streamwise velocity and $u_\infty$ the freestream velocity.

As shown in figure 6, velocity deficit rate drops from 0.6 to 0.1 between the two positions x/h=5 and x/h=40. Downstream this position, experimental results show that the deficit is located in the upper zone of the boundary layer and its value remains constant.

For turbulent boundary layers, theoretical work [28] and experimental studies [12] have shown that the maximum momentum deficit between the wake and

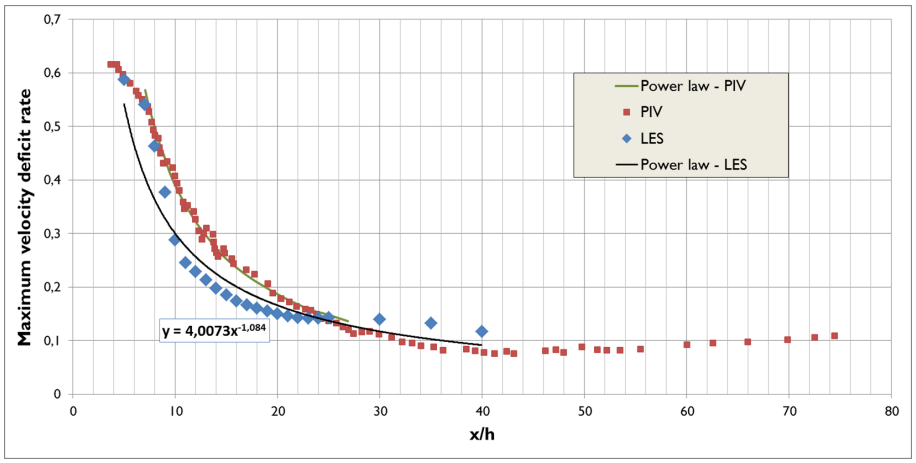


Figure 6: Streamwise evolution of maximum velocity deficit rate.

the free stream follows a power-law decay. The validity of this law has been verified by Ye *et al.*[18] for the micro-ramp roughness geometry in the range x/h=[7:27] that corresponds to a range dominated by swirling vortices.

The numerical momentum deficit rate is then computed from the present LES simulation results at different streamwise positions. A power-law fitting (black line) is done for the blue plot from figure 6 in the range x/h=[7:27] and is given by:

$$\frac{|\overline{u}(y) - \overline{u}_{BL}(y)|_{max}}{u_\infty} = 4.0073 \left(\frac{x}{h}\right)^{-1.084}. \tag{10}$$

The power exponent corresponds to the recovery rate of the momentum deficit. It is an indicator of the large-scale momentum mixing efficiency. The numerical recovery rate found with our numerical simulation 1.084 is close to the experimental value reported by Ye *et al.*[18] that is equal to 1.06, with a relative error of 2.3% which indicates a good agreement between both set of results which indicates a good agreement between both set of results.

## 4. Instantaneous flow

The instantaneous flow analysis is another important flow feature, because it is directly associated with the flow instability generated by the two main

vortices pairs. The instantaneous flow topology is expected to differ from the mean topology, as large scale fluctuations induced by the micro-ramp and the Kelvin-Helmholtz (K-H) instability takes place. The dynamic characterization of the roughness-induced transition phenomenon is carried out by inspecting the temporal and spatial evolution of coherent vortex structures. This can be achieved by using the well known $\lambda_2$ criterion [29], that allows the inspection of vortex organization within the flow. In order to highlight the accelerated and decelerated flow regions, and to allow a better comparison of numerial results with the experimental PIV data [14], the isocontours of $\lambda_2$ are coloured by streamwise velocity. The attached supplementary material (movie 1) shows the perspective view of the time-evolution instantaneous flow organization that is analyzed in the following paragraphs.

The results show that the backflow region behind the micro-ramp (x/h$\leq$4) is dominated by the trailing edge pair of vortices (TRP). The near-wake flow exhibits a quasi-steady behavior without any significant instabilities or fluctuations. Downstream this zone (x/h=5), Kelvin-Helmholtz instability mechanism appears and leads to the formation of vortex structures and fluctuations in the upper shear layer. These fluctuations are in agreement with the presence of a momentum deficit (inflection point) observed in figure 5.

As show in figure 7 by a detailed zoom near x/h=6, a primary hairpin vortex (PHV) system is formed. These structures are composed of a head portion (with a spanwise rotation) and a leg portion (quasi-streamwise rotation). While moving downstream, the swirling hairpin vortices are stretching and distorting. The hairpin vortices break down and their geometrical shape moves from hairpin to ring. The vortex structures lift up due to the upwash motion of the leg portion of the vortices. For a hairpin vortex system, the head breaks down and the feet of the structure connect together and form a full ring vortex (see figure 7(b)).

The upwash movement of the legs brings high-speed flow down and lifts up low-speed flow. Far from the roughness element (x/h=20-30), the formation of a new near-wall vortex systems due to interaction between low-momentum and outer flow fluid is observed. These lateral hairpin-shape secondary struc-

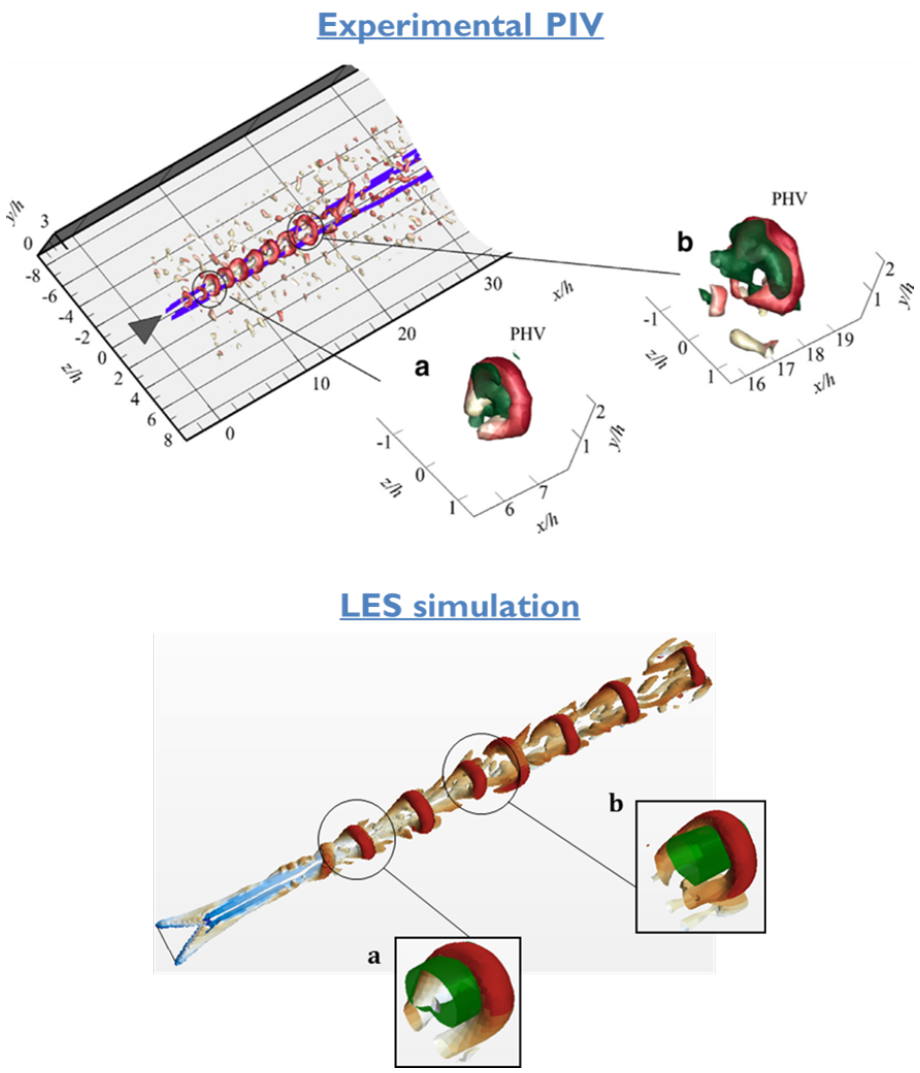


Figure 7: Instantaneous flow organization color coded by $u/u_\infty$ ; (a,b) perspective views at precise streamwise locations.

tures develop downstream while moving away from the symmetry plane z/h=0 and moving upward, forming a turbulent wedge. The interaction between the primary and secondary vortical structures is the mechanism that yields to the turbulence onset and a complex flow structure.

The coherent structures lead to an energy cascade, which ensures energy

transfer from the mean kinetic energy to the turbulent kinetic energy. The head portion of the primary hairpin vortices (PHV) contributes to the maximum peak of velocity fluctuations at the upper shear layer, as it will be shown in the next section in figure 8.

*Power spectrum.* Instantaneous visualizations from the LES simulations using the $\lambda_2$ criterion have been presented and analyzed in the previous section. The momentum deficit due to the shear layer modification showed to induce a flow instability, that leads to the creation of hairpin vortices. Now, the dynamic structures will be analyzed by visualizing the energy spectrum of the streamwise velocity component. The power spectral density is plotted versus the Strouhal number ($St = \frac{fh}{u_\infty}$) in figure 8. The probes 1 and 2 from figure 8(a) correspond to local points from the calculation domain located at (x/h=5h; y/h=1.25h; z/h=0) and (x/h=40h; y/h=1.25h; z/h=0), respectively.

At the probe 1 location, the flow is dominated by the formation of hairpin vortex structures. These unsteady structures appear as a single peak in the turbulence energy spectrum in figure 8(b). The Strouhal number associated with this main peak is equal to 0.242. The hairpin shedding Stouhal number (0.242) lies between 0.2 and 0.37, range reported by Acarlar and Smith [15] for a hemisphere protuberance in similar flow configuration.

The instantaneous visualizations presented in figure 7 suggest that the flow structures are much more complex at the probe 2 location than at the probe 1 location. According to energy spectrum analysis results, the magnitude of the peak in the power spectrum decreases while moving downstream. At probe 2 location, the vortex structures break down and flow interaction produce several secondary motions as previously depicted and thus a more disorganized distribution of flow perturbations and energy spectrum peaks are produced. Based on the energy spectrum in figure 8, it can be stated that the flow instability become non-linear at the probe 2 position and the flow behavior becomes turbulent.

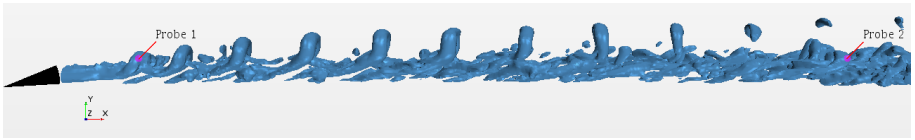


(a)

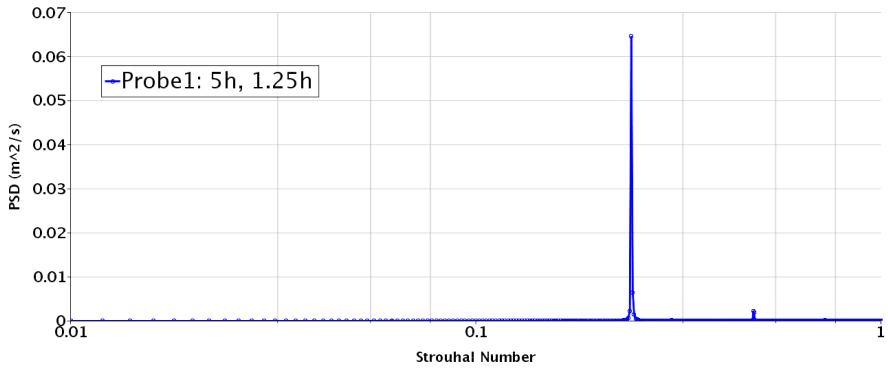


(b)

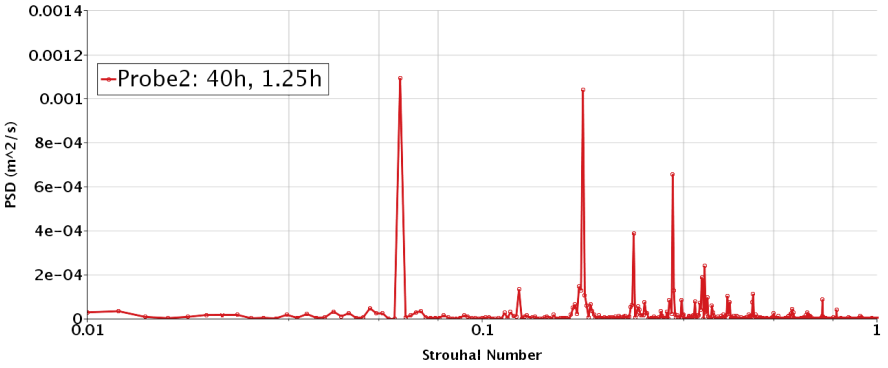


(c)

Figure 8: Energy spectrum analysis of the flow past a micro-ramp roughness with a laminar incoming boundary layer, at different positions x, y. a) schematic view of the probe positions. b) power spectral density for the probe 1 x=5h; y=1.25h. c) power spectral density for the probe 1 x=40h; y=1.25h.

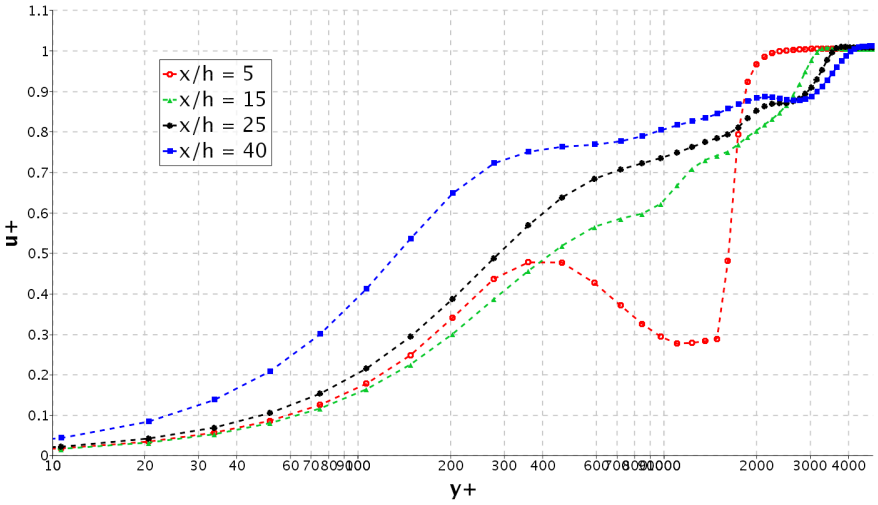


Figure 9: Semi-logarithmic non-dimensional velocity profiles at several streamwise positions

## 5. Turbulent properties

The dynamical characterization of the laminar-to-turbulent transition has been reported in the previous section by inspecting the evolution of coherent flow structures. According to the flow visualization, these structures might be related to an instability mechanism and contribute to velocity fluctuations. For that reason in this section, the appearance of oscillatory movements, their growth and the onset of turbulence will be represented and discussed through the velocity profiles, amplitude of streamwise velocity fluctuations and turbulence production.

### *5.1. Velocity profiles*

A possible way to detect the onset of tubulence is to plot the wall-normal semi-logarithmic velocity profiles. These profiles may be compared to the log-law profiles for turbulent boundary layer [30]. Mean velocity profiles along the symmetry plane are thus plotted versus the non-dimensional wall-normal position, see figure 9.

Turbulent boundary layer is characterized by a logarithmic law of the wall in the overlap region [31]:

$$u^+ = \frac{1}{\kappa} ln y^+ + B^+, \tag{11}$$

where $\kappa$ is the Von Kármán constant and $B^+$ a constant. $u^+$ is the dimensionless streamwise velocity and $y^+$ is the dimensionless distance to the wall. The results show that from x/h=5 to x/h=25, the velocity profiles exhibit a large deficit region. At x/h=40, the velocity profile become fuller and its upper part fits with a log-law profile in the range $y^+ \in [400 : 2000]$ corresponding to a straight line on the semi-log graph (figure 9). Thus, the velocity profile displays a logarithmic behavior that characterizes a turbulent state, at a distance of 40h downstream the obstacle.

*5.2. Velocity fluctuations*

The spatial distributions of the root mean square (RMS) values of streamwise velocity component are illustrated in figure 10 for several y-z cross-planes (x/h = 5, 15, 25 and 40). The RMS of the velocity fluctuations are good indicator of the turbulence intensity.

According to figure 10, peak velocity fluctuations are found to be located at the head portion of the coherent vortex structures (hairpin and ring) where the flow instability is produced. At x/h=5, a peak fluctuation is observed as a result of the upper shear layer instability (peak (I)). The RMS contours shape could be interpreted as the elongated hairpin vortices formed downstream the roughness element. The concentrated RMS values locations are the zones where the local velocity profile has an inflection point in the wall-normal direction, that is, $\frac{\partial^2 \overline{u}}{\partial y^2} = 0$. It indicates that the fluctuations result from a Kelvin-Helmholtz-type instability mechanism in the wall-normal direction. The maximum of velocity fluctuations lifts up due the primary vortices upwash motion when moving downstream the obstacle. Also, the fluctuations magnitude is decreased due to the recovery process. Furthermore it can be seen that beneath the primary region at x/h=15, the downwash movement of secondary vortices transports high

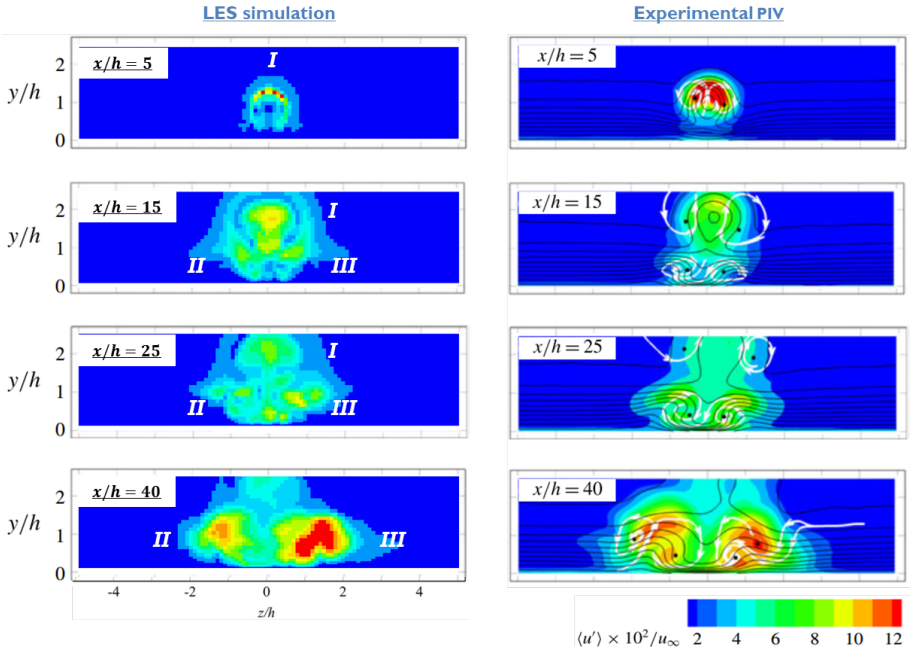


Figure 10: Cross-sectional contours of streamwise velocity fluctuations.

momentum fluid to the wall which increases the velocity fluctuations (peaks (II) and (III)). Moving further downstream, we observe a persistence of the secondary turbulence peaks where the head appears to have dissipated. The fluctuations are stronger and cover a wider spanwise region (lateral propagation). A turbulent wedge originating at the roughness is produced, where large-scale hairpin vortices transfer mean flow energy into turbulence. Thus, it promotes the laminar-to-turbulent transition.

It can be stated from the spatial distribution of the streamwise velocity fluctuations that region of maximum RMS intensity is less spread by LES at x/h=5 and the RMS intensity is slightly overestimated by LES at x/h=40 compared to tomographic PIV data [18].

## 6. Conclusion

In this contribution, Large-Eddy Simulations (LES) were carried out to investigate the induced transitional flow phenomenon over a ramp-type wall-mounted roughness element immersed in a developing boundary layer at a supercritical regime. The results present several transition flow features that are compared to tomographic PIV experimental data from [14, 18]. The comparisons show that the present LES methodology is well adapted for this type of transitional flow, and makes it possible to account numerically for the various physical phenomenon involved.

The mean flow analysis indicates the formation of a primary contra-rotating pair of vortices (TRP) at the trailing edge of the obstacle, which consequently generates an upwash motion and a streamwise momentum deficit. The shear layer becomes unstable, and a hairpin-like vortex system is generated due to Kelvin-Helmholtz type instability. These vortices are formed in the near-wake of the micro-ramp, and are stretched when moving downstream. A second pair of vortices is formed in the near-wall. The break down of the primary hairpin system produces new near-wall vortices propagating in the spanwise direction. The head of the hairpin vortices and the secondary vortices are found to generate a local high-turbulence zones, associated with the velocity fluctuations.

In our study, the instantaneous flow topology shows that the flow downstream the obstacle is dominated by Kelvin-Hemholtz vortices, which are generated in the form of hairpin. A study of the velocity fluctuations shows that the maximum values of turbulence production are concentrated at the head of the haiprin vortex structures, and at the edges of the turbulent wake created downstream of the obstacle. The coherent structures are mainly organized into hairpin vortices shed from the near-roughness wake region and wall-attached vortices generated at both sides of the micro-ramp wake.

The streamwise mean velocity, turbulent fluctuations and instantaneous vortex visualization are in relatively good agreement with experiments. A discrepancy in the streamwise turbulent fluctuations intensity is observed, and can be

ascribed to the experimental PIV resolution, the discretization scheme and the subgrid scale model.

The boundary layer induced-transition phenomenon past an immersed micro-ramp can then be summarized in four main stages:

- Formation of longitudinal vortices in the very near wake of the obstacle with a quasi-steady shear flow.
- Development of Kelvin-Helmholtz instabilities and formation of transverse hairpin vortex structures.
- Evolution of vortices to a hairpin or ring shape, and vortex merging.
- Generation of new vortex structures in the near-wall and lateral propagation (turbulent wedge).

The boundary layer transition is therefore associated with the modified shear layer induced by the vortices past the obstacle, as well as the inflectional velocity profile.

It would be fruitful to pursue further research about the effect of an immersed roughness element placed in laminar flow on a heated plate in order to assess the thermal enhancement of a such configuration.

## References


[1] I. Tani, Boundary-layer transition, Annual Review of Fluid Mechanics 1 (1) (1969) 169–196. arXiv:https://doi.org/10.1146/annurev.fl.01.010169.001125, doi:10.1146/annurev.fl.01.010169.001125.
URL https://doi.org/10.1146/annurev.fl.01.010169.001125

[2] I. Tani, Boundary-layer transition by isolated roughness, Aeronautical Research Institute (1962) 129–143arXiv:https://doi.org/10.1146/annurev.fl.01.010169.001125, doi:10.1146/annurev.fl.01.010169.001125.
URL https://doi.org/10.1146/annurev.fl.01.010169.001125

[3] A. E. Von Doenhoff, A. L. Braslow, The effect of distributed surface roughness on laminar flow, Boundary Layer and Flow Control (1961) 657–681.

[4] D. Corson, R. Jaiman, F. Shakib, Industrial application of rans modelling: capabilities and needs, International Journal of Computational Fluid Dynamics 23 (4) (2009) 337–347. arXiv:https://doi.org/10.1080/10618560902776810, doi:10.1080/10618560902776810.
URL https://doi.org/10.1080/10618560902776810

[5] W. H. Shia-Hui Peng, Piotr Doerffer (Ed.), Progress in Hybrid RANS-LES Modelling, Notes on Numerical Fluid Mechanics and Multidisciplinary Design, Springer, Berlin, Heidelberg, 2009. doi:10.1007/978-3-642-14168-3.

[6] E. Toubiana, S. Russeil, D. Bougeard, N. Francois, Large eddy simulation and reynolds-averaged navier stokes modeling of flow in staggered plate arrays: Comparison at various flow regimes, Applied Thermal Engineering 89 (2015) 405 – 420. doi:https://doi.org/10.1016/j.applthermaleng.2015.06.025.
URL http://www.sciencedirect.com/science/article/pii/S1359431115005797

[7] L.-Z. Zhang, W.-C. Zhong, J.-M. Chen, J.-R. Zhou, Fluid flow and heat transfer in plate-fin and tube heat exchangers in a transitional flow regime, Numerical Heat Transfer, Part A: Applications 60 (9) (2011) 766–784. arXiv:https://doi.org/10.1080/10407782.2011.627802, doi:10.1080/10407782.2011.627802.
URL https://doi.org/10.1080/10407782.2011.627802

[8] P. Malan, K. Suluksna, E. Juntasaro, Calibrating the Gamma-Re_theta Transition Model for Commercial CFD, Aerospace Sciences Meetings, American Institute of Aeronautics and Astronautics, 2009, 0. doi:10.2514/6.2009-1142.
URL https://doi.org/10.2514/6.2009-1142

[9] F. R. Menter, Two-equation eddy-viscosity turbulence models for engineering applications, AIAA Journal 32 (8) (1994) 1598–1605. doi:10.2514/3.12149.
URL https://doi.org/10.2514/3.12149

[10] S. C. Tirtey, O. Chazot, L. Walpot, Characterization of hypersonic roughness-induced boundary-layer transition, Experiments in Fluids 50 (2) (2011) 407–418. doi:10.1007/s00348-010-0939-4.
URL https://doi.org/10.1007/s00348-010-0939-4

[11] Z. Sun, F. Scarano, B. W. van Oudheusden, F. F. J. Schrijer, Y. Yan, C. Liu, Numerical and experimental investigations of the supersonic microramp wake, AIAA Journal 52 (7) (2014) 1518–1527. doi:10.2514/1.J052649.
URL https://doi.org/10.2514/1.J052649

[12] Z. Sun, F. F. J. Schrijer, F. Scarano, B. W. van Oudheusden, Decay of the supersonic turbulent wakes from micro-ramps, Physics of Fluids 26 (2) (2014) 025115. doi:https://doi.org/10.1063/1.4866012.

[13] S. K. Robinson, Coherent motions in the turbulent boundary layer, Annual Review of Fluid Mechanics 23 (1) (1991) 601–639. arXiv:https://doi.org/10.1146/annurev.fl.23.010191.003125, doi:10.1146/annurev.fl.23.010191.003125.
URL https://doi.org/10.1146/annurev.fl.23.010191.003125

[14] Q. Ye, F. F. J. Schrijer, F. Scarano, Geometry effect of isolated roughness on boundary layer transition investigated by tomographic piv, International Journal of Heat and Fluid Flow 61 (2016) 31–44. doi:10.1016/j.ijheatfluidflow.2016.05.016.

[15] M. S. Acarlar, C. R. Smith, A study of hairpin vortices in a laminar boundary layer. part 1. hairpin vortices generated by a hemisphere protuberance, Journal of Fluid Mechanics 175 (1987) 1–41. doi:10.1017/S0022112087000272.

[16] H. Yanaoka, T. Inamura, S. Kawabe, Turbulence and heat transfer of a hairpin vortex formed behind a cube in a laminar boundary layer, Numerical Heat Transfer, Part A: Applications 52 (11) (2007) 973–990. arXiv:https://doi.org/10.1080/10407780701389590, doi:10.1080/10407780701389590.
URL https://doi.org/10.1080/10407780701389590

[17] C. Diaz-Daniel, S. Laizet, J. Vassilicos, Direct numerical simulations of a wall-attached cube immersed in laminar and turbulent boundary layers, International Journal of Heat and Fluid Flow 68 (2017) 269 – 280. doi:https://doi.org/10.1016/j.ijheatfluidflow.2017.09.015.
URL http://www.sciencedirect.com/science/article/pii/S0142727X17303995

[18] Q. Ye, F. F. J. Schrijer, F. Scarano, Boundary layer transition mechanisms behind a micro-ramp, Journal of Fluid Mechanics 793 (2016) 132–161.

[19] O. Zikanov, Essential Computational Fluid Dynamics, Wiley, 2010.
URL https://books.google.fr/books?id=e7fR2yu3HvQC

[20] F. Nicoud, F. Ducros, Subgrid-scale stress modelling based on the square of the velocity gradient tensor, Flow, Turbulence and Combustion 62 (1999) 183–200.

[21] Q. Ye, F. F. J. Schrijer, F. Scarano, On reynolds number dependence of micro-ramp-induced transition, Journal of Fluid Mechanics 837 (2018) 597626. doi:10.1017/jfm.2017.840.

[22] H. Schlichting, K. Gersten, Boundary-layer theory, McGraw-hill New York, 1955.

[23] S. P. Software, User guide Star-CCM+ version 12.02 (2017).

[24] I. Celik, Z. Cehreli, I. Yavuz, Index of resolution quality for large eddy simulations, Journal of fluids engineering 127 (5) (2005) 949–958.

[25] S. B. Pope, Ten questions concerning the large-eddy simulation of turbulent flows, New journal of Physics 6(1) (2004) 35.

[26] S. B. Pope, Turbulent flows, Cambridge University Press, 2001.

[27] H. K. Versteeg, W. Malalasekera, An introduction to computational fluid dynamics: the finite volume method, Pearson Education, 2007.

[28] H. Tennekes, J. L. Lumley, A first course in turbulence, MIT Press, 1972.

[29] F. Jeong, J. Hussain, On the identification of a vortex, Journal of fluid mechanics 285 (1995) 69–94.

[30] D. E. Coles, Computation of turbulent boundary layers, in: 1968 AFOSR-IFP-Stanford Conference, 1969.

[31] T. Von Kármán, Mechanical similitude and turbulence.